

Crosstalk-mitigated microelectronic control for optically-active spins

Hao-Cheng Weng^{1*}, John G. Rarity¹, Krishna C. Balram¹, Joe A. Smith^{1*}

¹Quantum Engineering Technology Labs, H. H. Wills Physics Laboratory and Department of Electrical and Electronic Engineering, University of Bristol, Bristol BS8 1TL, United Kingdom.

*Corresponding author(s). E-mail(s): haocheng.weng@bristol.ac.uk; j.smith@bristol.ac.uk;

Abstract

To exploit the sub-nanometre dimensions of qubits for large-scale quantum information processing, corresponding control architectures require both energy and space efficiency, with the on-chip footprint of unit-cell electronics ideally micron-scale. However, the spin coherence of qubits in close packing is severely deteriorated by microwave crosstalk from neighbouring control sites. Here, we present a crosstalk-mitigation scheme using foundry microelectronics, to address solid-state spins at sub-100 μm spacing without the need for qubit-detuning. Using nitrogen-vacancy centres in nanodiamonds as qubit prototypes, we first demonstrate 10 MHz Rabi oscillation at milliwatts of microwave power. Implementing the active cancellation, we then prove that the crosstalk field from neighbouring lattice sites can be reduced to undetectable levels. We finally extend the scheme to show increased qubit control, tripling the spin coherence under crosstalk mitigation. Compatible with integrated optics, our results present a step towards scalable control across quantum platforms using silicon microelectronics.

Keywords: Microwave crosstalk, Microelectronics, Large-scale quantum systems, Chip integration, Solid-state spins, Nitrogen-Vacancy centres

The field of quantum computing, underscored by demonstrations of computational quantum advantages [1, 2], has shifted towards engineering scalable systems, both in terms of qubit quality [3] and quantity [4]. To scale up, the key advantage of solid-state systems is the prospect of achieving close packing of qubits considering energy efficiency and space constraints in cryogenic operations. However, for large-scale systems, performance becomes limited by classical control and wiring [5, 6], especially when close packing brings with it the problem of qubit crosstalk between neighbouring controls. A crosstalk-free electronic architecture is therefore required in which qubits and their associated control lines scale with forward compatibility.

A variety of control signals for quantum systems fall in the megahertz to gigahertz-frequency domain [7, 8]. These systems range from superconducting transmon qubits to spin qubits in solid-state systems and trapped ions [9–11] where two-level systems are addressed by microwave pulses. Progress on crosstalk mitigation has been made particularly in superconducting qubits [12], however these designs are not directly adaptable to qubits with optical access such as colour centres in diamond, 2D materials, and trapped ions. Close proximity

of metallic structures to optics enhances scattering and loss of photons, posing a significant challenge. Previous work in trapped ions [13] employed gradient fields to give unique frequency addressability to each qubit, preventing crosstalk. For solid-state defects, recent work proposed alternative spin driving schemes with strain-tunable electrodes [14] and electromechanical control [15] to achieve localised control fields. Nevertheless, requiring distinct microwave frequencies per qubit is experimentally costly and mechanical control is challenging to fabricate.

In this work, we present a new design for site-defined control with silicon microelectronics, prototyping with foundry Application-Specific Integrated Circuits (ASIC) and nitrogen-vacancy centres in diamonds (NVs). NVs are well-characterised spin qubits with optical interfaces [16–18]. Moreover, the room-temperature operation of NV spin systems and point-like localisation makes them ideal prototypes for testing large-scale control architectures in the gigahertz regime. By exploiting the complexity of microelectronics, we introduce a dual-loop transducer which effectively isolates single control sites at sub-100 μm

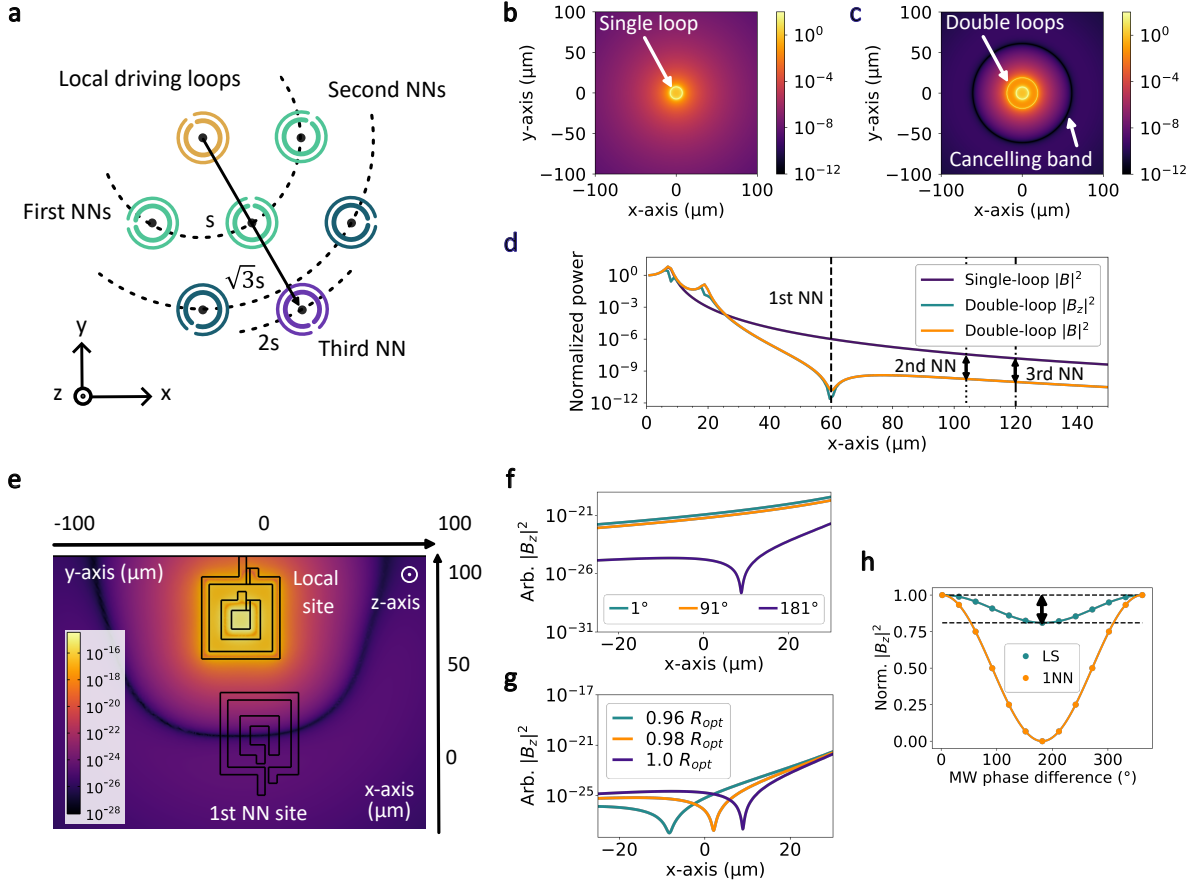


Fig. 1 Active crosstalk cancellation scheme. **a** Hexagonal packing of driving sites: to the upper-left (golden) site, the sites in light green are first Nearest Neighbour (NN) sites at a distance of s . The second (in dark green) and third NN sites (in purple) are $\sqrt{3}s$ and $2s$ away, respectively. Each site is presented by two concentric loops hosting a spin qubit (black dot in the centre) set in the x-y plane, where the outer loop produces a cancelling signal out-of-phase with the inner loop signal. **b-c** Plots of the magnetic power out of the plane ($|B_z|^2$ at $z = 1 \mu\text{m}$ above the plane) at the driving site in the single/double loop scheme. The power is normalized w.r.t. that at the loop centre. **d** Comparison of the magnetic field power along the x-axis ($y = 0$), showing field cancellation. The power attenuation at second and third NN sites is labelled. **e** Finite-element simulation of this structure realised following foundry microelectronics design rules. The outer loops are $38 \mu\text{m}$ in diameter and the inner loops $15.5 \mu\text{m}$. The power of the out-of-plane magnetic field component $|B_z|^2$ is plotted. **f** The field cancellation shown precisely when the phase difference (lines in graph) is at 181° in the simulation. **g** The point of maximal cancellation spatially tuned by changing the driving ratio R_{opt} between the two loops. **h** Comparison of the driving power $|B_z|^2$ at the local site (LS) and the first NN site (1NN), in a sweep of set microwave phase difference between the inner and outer loop.

qubit packing densities. Our result illustrates the possibility of scalable control for spins individually and simultaneously in a compact device. The scheme is scalable and paves the way for further combination with active microelectronics and integrated optics.

Active crosstalk cancellation

Spin-based quantum systems are commonly electrically driven by a close metallic structure to ensure efficient manipulation. However, for optically-active spins, this structure should be located at least several optical wavelengths away from the spin, to prevent optical scattering and loss in the photonic channel. Therefore, there is a trade-off between the deliverable field at the spin and the need to reduce optical loss. To account for this, we introduce a circular loop geometry (in Fig.1a) for dedicated spin control of each site. This maximises the area into which photonic structures

can be introduced, whilst also maximising the contact area of the driving transducer for a concentrated and directed field.

On the other hand, as microwave controls for spin systems have a near infinite wavelength $\lambda > 1 \text{ cm}$, compared to micrometre features, their spatial extent can be significant, deleteriously affecting secondary systems located nearby. As an example, in Fig.1b, a $15 \mu\text{m}$ diameter loop on the x-y plane (as the coordinate in Fig.1a) is presented by the magnetic power out of the plane ($|B_z|^2$). The calculation follows an analytical model describing the magnetic field of current carrying loops (Supplementary Section A). The loop delivers 0 dB power to the control site at the origin and a significant power (-60dB or 0.5% reduction in the spin coherence time, Supplementary Section I) remains at $60 \mu\text{m}$ from the centre (purple line in Fig.1d). Common methods to remove the residual field, such as enclosing

Faraday cages or lead shielding, are incompatible with planar fabrication processes.

However, by adopting multi-layer metallisation from silicon microelectronics, we have the flexibility to route signals out of the plane, enabling complex geometries. In this work, we exploit this by considering two lithographically-defined concentric loops, as shown in Fig.1a. By driving the two loops 180° out-of-phase, the two counter-propagating fields cancel out, away from the local control site. Compared to the single loop in Fig.1b, Fig.1c plots the field power ($|B_z|^2$) of the two-loop model, with an outer loop of diameter $38\ \mu\text{m}$ added. This design allows (i) a much more localised field and (ii) precisely cancelling of the field at a distance corresponding to the first Nearest Neighbour (NN) sites. This is achieved by setting the current in the outer loop such that the field strength at the cancelling point is equal and opposite to that from the inner loop. In the plot, a fast spatial decay of field is observed with a band of maximal cancellation. The scheme scales for all NN sites at the same distance from the local site. Also, as long as the cancelling condition holds, the scheme works with any driving field (of difference set phase or pulse width).

In Fig.1d, we plot the total magnetic power $|B|^2$ (normalised to the control site at $x = 0$) at NN sites spaced with hexagonal packing (depicted in Fig.1a with $s = 60\ \mu\text{m}$). In the two-loop scheme, the field cancels perfectly at the first NN site ($x = 60\ \mu\text{m}$), showing high power extinction (-120 dB, when 0 db is delivered at $x = 0$), or equivalently an additional -50 dB attenuation compared to the single-loop case. As the dominant field component is in the z-direction, the two-loop $|B|^2$ extinction ratio is similar to that of $|B_z|^2$. At the second and third NN sites ($x = 104\ \mu\text{m}$ and $x = 120\ \mu\text{m}$), as the field decays faster in the two-loop scheme (following a $1/x^{15}$ power law decay as compared to the $1/x^6$ for the single-loop scheme when fitted), an additional -20 dB power attenuation is applied. It is worth noting that the double-loop driving does not diminish the field at the host centre ($x = 0$ in Fig.1d) as compared to the single loop case. This is because the power from the inner loop is 6.3 times stronger compared to the outer loop at the host centre, due to its proximity to the spin (see Supplementary Section B for the power law relation).

Considering the design in Fig.1c now with finite-width current carrying wires and a rectangular geometry, we examine the cancellation in a fabricable device through a gigahertz finite-element simulation (Supplementary Section B). In Fig.1e, we show the magnetic field power ($|B_z|^2$) on this device containing a local driving site and a first NN site. By setting the driving current ratio and phase difference, the maximally cancelled region forms a band as with the analytical model in Fig.1c. In Fig.1f, by tuning the relative phase

between the feeds driving each loop, complete cancellation happens at 181° , producing -50 dB attenuation at the first NN ($x=10\ \mu\text{m}$ following the coordinates in Fig.1e). This attenuation follows that observed in Fig.1c. The cancelling point can be fine tuned spatially by changing the driving ratio between the two loops. In Fig.1g, by sweeping the driving voltage ratio between the inner and outer loops at the local site R around R_{opt} , the optimised ratio such that cancelling happens at $x = 10\ \mu\text{m}$, the dip can be tuned between $x = 0$ to $20\ \mu\text{m}$.

In Fig.1h, we compare the field at the local site centre (top of Fig.1e) and the remote site (bottom). Along the phase sweep, only a slight reduction in power ($< 20\%$) is observed at the local site. This allows the cancelling scheme to operate without significantly sacrificing the local driving field. In practice, once the cancellation condition is found, the microwave source amplitude can be scaled to achieve a desired driving power.

Hybrid device realisation

To demonstrate the active crosstalk cancellation in a scalable platform, we leverage a commercial $0.13\ \mu\text{m}$ back-end-of-line silicon foundry process with aluminium layers, isolated with silicon dioxide, and tungsten vias (see Methods). In Fig.2a, the structure is realised in two rectangular loops of the same dimensions as Fig.1e. As a demonstration, nanodiamonds containing single optically-accessible NVs are lithographically positioned in a post-processing step (Fig.2b, see also Methods). The structure imaged using scanning electron microscopy is shown in Fig.2c. The hybrid device is studied with confocal microscopy under $515\ \text{nm}$ laser excitation to identify an isolated NV at the control site (Fig.2c) through photoluminescence (PL).

By controlling the NV in Fig.2c, we can evaluate the microelectronics performance for manipulating a quantum system. We perform Rabi oscillations on the NV electron spin (see Methods) by applying microwave and laser pulses presented in Fig.3a. As the microwave pulse width τ is swept, the oscillation of PL intensity reveals the spin state transition at a frequency f_{Rabi} proportional to the square root of microwave power applied. We compare the Rabi oscillation of the same NV when driven with the on-chip left outer loops (Fig.3b-d), right outer loops (Fig.3e-g) to a typical Printed Circuit Board (PCB) antenna [19] (Fig.3h-j), following the labels in Fig.2a.

In Fig.3k, plotting the power dependence of the observed Rabi frequency indicates that on-chip driving is significantly more efficient, as expected from the micron proximity to the radiation source (following the $1/r^3$ power law decay where r is distance from the source), as opposed to approximately $500\ \mu\text{m}$ for the external antenna (Fig.3l). Specifically, our result

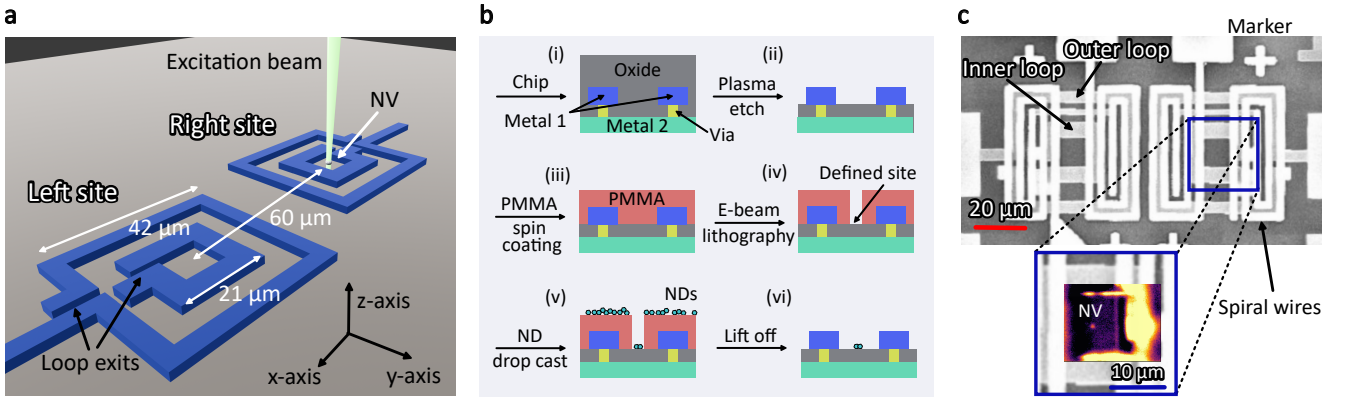


Fig. 2 Hybrid microelectronic device. **a** Schematic of the hybrid device showing the dual-loop structures realised on an ASIC, combined with an Nitrogen-Vacancy centre (NV) in a nanodiamond. The dimensions of inner/outer loops follow that simulated in Fig.1e. The right site shows the NV in the positioned nanodiamond addressed by the excitation laser. **b** Fabrication steps of nanodiamond (ND) positioning using a PMMA resist (see Methods). The multi-layer (Metal 1 and Metal 2) device cross section is shown with interconnecting vias and capped with silicon oxide. **c** An exemplar scanning electron microscope image of the device. Markers are used during the positioning process for alignment. The loop structures are underneath spiral wires not used in the current experiment. The inset shows a confocal scan of the optically-active NV (shown by the central Gaussian spot) in the centre of the structure.

shows that the on-chip metallic loop interface can be two hundred times more efficient, achieving a Rabi frequency $f_{Rabi} \simeq 10$ MHz with 50 mW (power at the loop). This is fast enough for coherent control of the NV electron spin considering $1/f_{Rabi} < T_2/10$ where the typical T_2 coherence time for NV electron spin in nanodiamond is around $1 \mu\text{s}$ [20]. It is worth noting that more efficient driving has been achieved by identifying NVs close to patterned metallisation on diamond [21] or nearby wires [22]. However, our demonstration presents a scalable solution with foundry microelectronics, providing both the uniformity of field in the loop to favour NV positioning and compatibility with integrated photonics.

Crosstalk-mitigated spin control

With the ability to efficiently manipulate the spin, we progress to demonstrate the crosstalk mitigation scheme. By operating both the inner and outer loops (left site in Fig.2a) at the site adjacent to the isolated spin site, our aim is to observe the cancellation of the driving field from this neighbouring control site, at the position of the isolated spin.

The cancellation condition can be found experimentally by first balancing the effect of the driving fields from the inner and outer loops on the NV spin. The driving field strength can be inferred from continuous-wave Optically Detected Magnetic Resonance (ODMR) measurements (see Methods). In ODMR, when the microwave source frequency is swept, a dip with a certain depth, the ODMR contrast, is observed at the resonance of the spin state transition. In the low pump regime (small microwave power) [23], this contrast is proportional to the microwave power. In Fig.4a, we calibrate this linearity and demonstrate

that the ODMR contrast can be directly used to quantify the microwave power measured at the NV site. The phase shifter, through which the microwave phase difference between the inner and outer loops is applied, is also calibrated to exclude change in microwave power dependent on the set phase. When the left outer loop is driven alone, Fig.4b shows that changes of ODMR contrast are within error bars.

Once the driving fields are balanced, with both loops activated, one needs to identify the set phase between the microwaves applied to the loops. In Fig.4c, we observe the sinusoidal relation between the applied phase difference and the ODMR contrast, as expected in Fig.1h. The cancelling phase condition is then the destructive interference point (45°) where the contrast approaches its minimum. In Fig.4d and Fig.4e, the destructive interference (at 45°) shows an undetectable dip within the error bar, while the constructive interference (at 225°) is seen with the highest contrast dip at 3.14 GHz. From the fitting in Fig.4c, the minimum point shows a normalised power of 0.06 ± 0.06 , meaning that the microwave power is undetectable within error bars.

Under this crosstalk-mitigation condition, we can now demonstrate coherent spin control. Our scheme considers two adjacent control sites with associated qubits, Q_L and Q_R , shown in Fig.4f). Microwave control for Q_L is allowed to perform arbitrary single qubit rotations on the spin two-level system, whilst independently, Q_R is coherently controlled and evaluated. The crosstalk-mitigated control of Q_R (by cancelling the crosstalk field from the other site) means that the control of Q_R will remain coherent, independent of the control signal for Q_L . Otherwise, the microwave crosstalk would result in random rotations on Q_L , diminishing the ability to perform coherent qubit control.

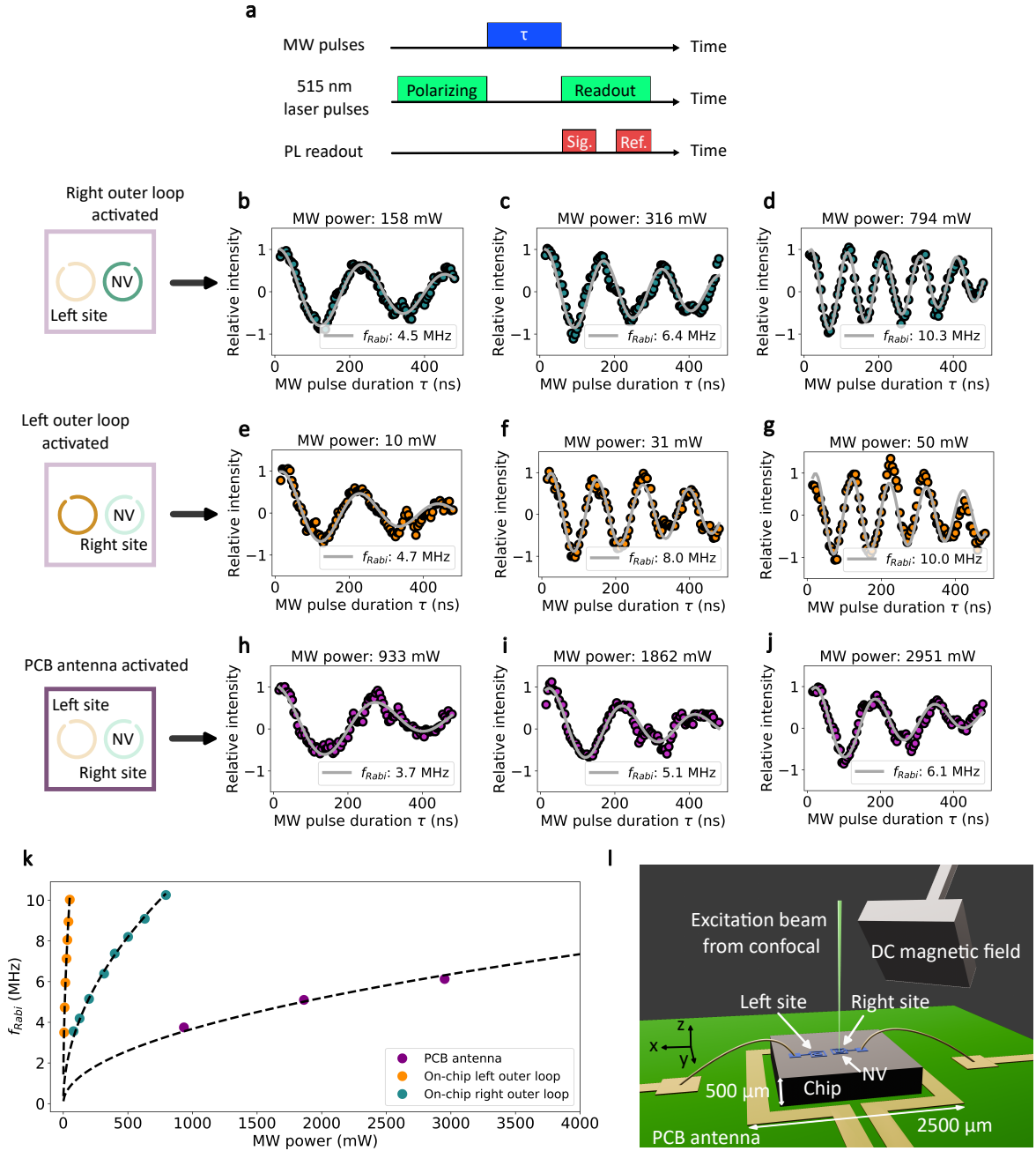


Fig. 3 On-chip electron spin driving. **a** Pulse sequences for Rabi oscillation experiments. The first part of the photoluminescence (PL) readout is the signal (Sig.) that contributes to the state-dependent intensity contrast and the second part is a reference (Ref.) for normalisation of counts. The metallic loops are studied by performing Rabi oscillations on the same NV electron spin. The spin associated with the isolated NV is driven by the on-chip right outer loop (**b-d** in green), the on-chip left outer loop (**e-g** in orange), and an external circuit board antenna (**h-j** in purple), showing the Rabi oscillation. The applied microwave (MW) power and Rabi frequency are labelled. Here, the microwave power is normalised to the loop S_{11} incoefficient, i.e., the microwave reflection coefficient (Supplementary Section E), representing the power delivered by the loop structures. **k** Comparing the on-chip loop structures to the global PCB antenna demonstrates an observed two-hundred fold improvement in driving efficiency above 10 MHz. Lower efficiency from the right outer loop is due to losses experimentally observed (Supplementary Fig.S5). **l** A schematic diagram showing the spatial relations between the on-chip loops and the PCB antenna. Dimensions are not to scale.

For Q_L , the arbitrary rotations $R_{\vec{r}_n}(\phi_n)$ corresponds to resonant microwave pulses of different phases, starting time, and end time. Randomly chosen rotations can thus be simulated by a resonant microwave signal (at 3.14 GHz) in continuous wave (considering that random pulsing would average out in time) with randomly changing phases. We deliver

the same signal to the left inner and outer loop (labelled in Fig.2a) with the Π phase shift for the cancelling condition to hold (Supplementary Section H). Pulse sequences are shown in Fig.4g. Rabi sequences (microwave pulses of variable length τ) are then delivered to the right outer loop (similar to Fig.3a).

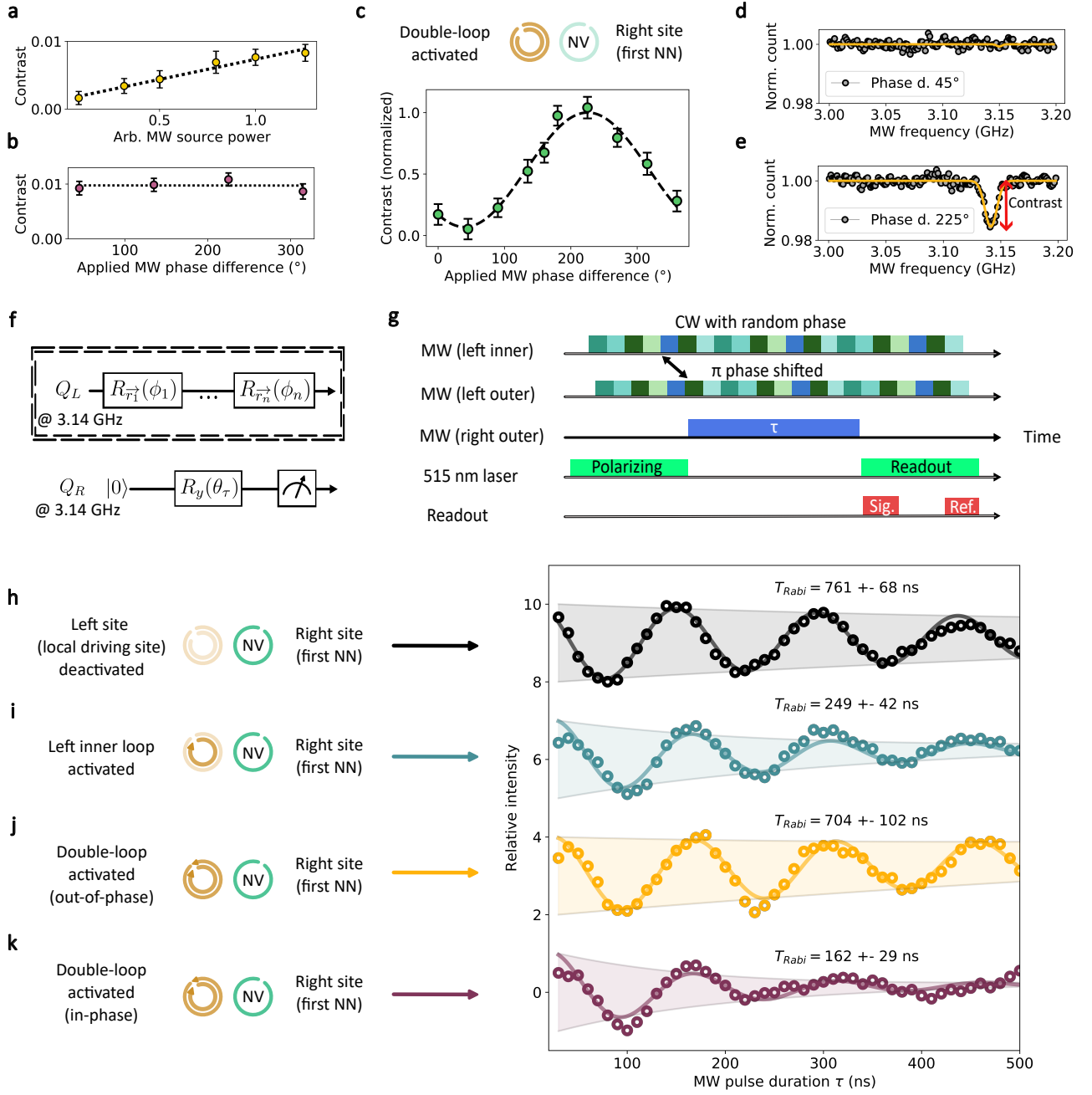


Fig. 4 Active crosstalk cancelling. **a** The Optically Detected Magnetic Resonance (ODMR) contrast observed in linear relation to the microwave (MW) power for spin driving. **b** The phase shifter calibration, with negligible change observed (within error bars) in ODMR contrast across different set phase. **c** Under the two-loop driving, a sinusoidal relation between the ODMR contrast and the applied phase difference between the two loop feeds is observed. **d-e** The ODMR measurement when the applied microwave phase difference (abbreviated as phase d.) is 45° (225°), showing minimal (maximal) ODMR contrast. **f** Gate sequences for the crosstalk-mitigated spin manipulation, considering two qubits Q_L and Q_R . Random qubit rotations $R_{\vec{r}_n}(\phi_n)$ (rotation around the y-axis on the qubit Bloch sphere) performed on Q_L and $R_y(\theta_{\tau})$ (rotation around the y-axis on the qubit Bloch sphere) performed on Q_R before state readout. Here, both qubits operate at 3.14 GHz. **g** Corresponding pulse sequences for demonstrating the crosstalk-mitigated spin manipulation. Microwave pulses in different colors (top two rows) corresponds to different phases. Here, a random phase is applied every second over the > 3 hour accumulation time for each experiment. The Rabi sequence follows that performed in Fig.3a. The microwave power applied to the left loops are larger than that to the right loop, allowing a clear observation of spin decoherence under noise. **h** Rabi oscillations driving only the right outer loop. The data is presented with a sinusoidal fitting and corresponding T_{Rabi} . **i** Rabi oscillations with the left inner loop also driving, showing reduced control of spin qubit. **j** Rabi oscillations protected by the two-loop active cancelling scheme (driving out of phase), showing regained control. **k** Rabi oscillations when the two left loops are in phase, showing increased crosstalk.

With the microwave signal in Fig.4g applied, we compare the quantum control of Q_R under different

conditions. Fig.4h shows the Rabi oscillation performed by the right outer loop alone, serving as a

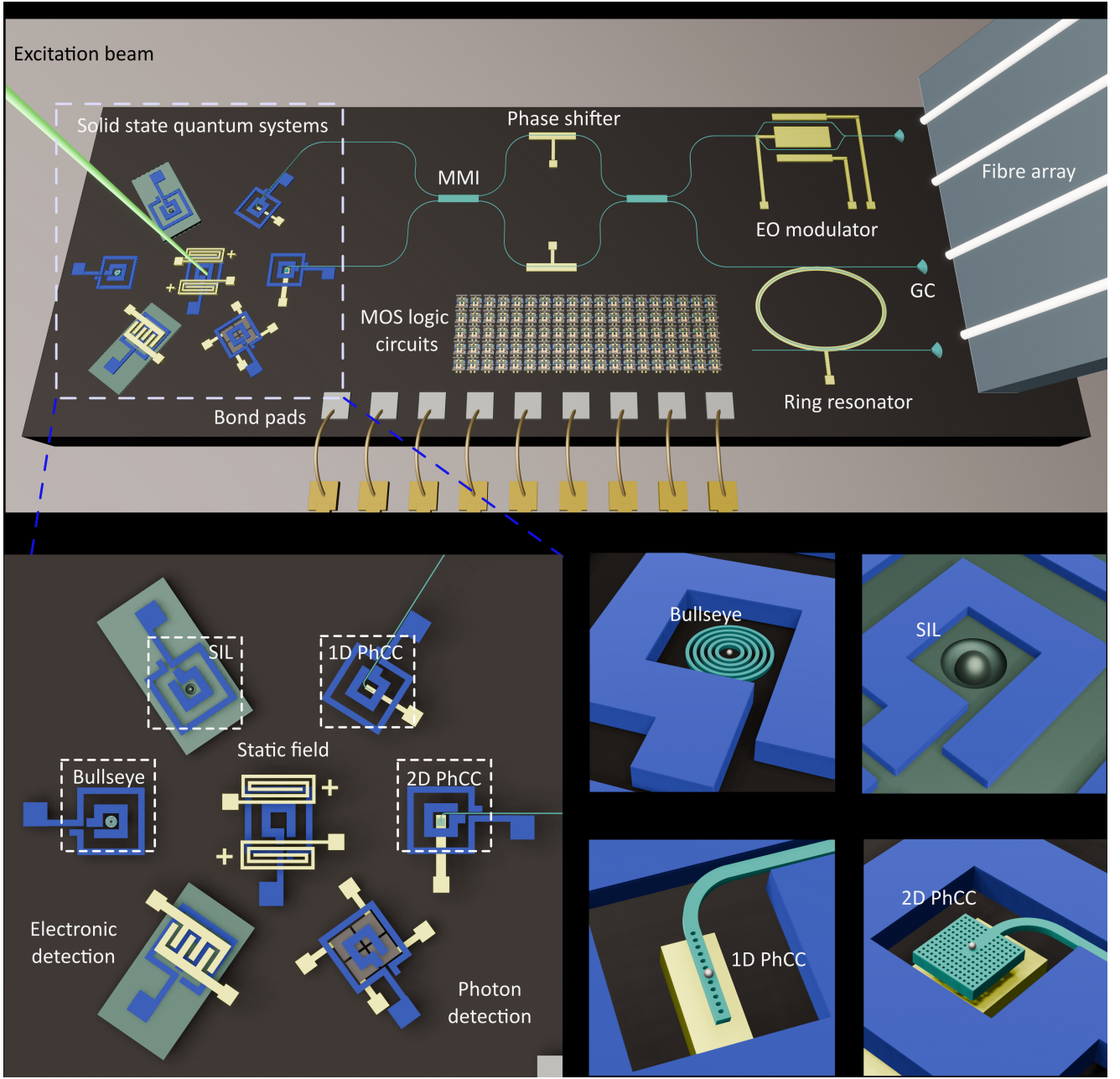


Fig. 5 Schematic device of electronic and photonic integration for solid-state spins. **a** The schematic device. The left part of the device presents integration of solid-state spins with photonics and electronics. The upper part shows a Mach-Zehnder interferometer (by combining two multimode interferometers (MMI) and a phase shifter) that entangles photons, an electro-optical modulator (EO modulator) for fast switching, ring resonators for spectral filtering, and grating couplers (GC) for optical input/output through a fibre array. The lower part of the device contains silicon logic circuits (NAND gates as an example) that can be used for on-chip decision and control across the device. Bond pads at the bottom provide electrical I/O connections. **b** The left part of the device zoomed in. Seven sites of the two-loop metallic structures are distributed in the hexagonal packaging as shown in Fig.1a. Beyond the loops, each site presents a possible hybrid integration of photonics and electronics for the hosted solid-state quantum system. From upper left (clock-wise) and lastly the centre, we show photonic integration to Solid Immersion Lenses (SIL) fabricated on thin film diamond, nanodiamonds in a 1D photonic crystal cavity (1D PhCC), 2D photonic crystal cavity (2D PhCC) with phase shifter, nanodiamonds positioned on photodiodes for photon detection, electrical spin state readout of NVs in thin film diamond, nanodiamonds at the centre of bullseye gratings, and spiral wires around the spin for resonance tuning through static magnetic field. **c-f** The photonic integration with metallic loops zoomed in: bullseye gratings, solid immersion lens, 1D photonic crystal cavity, and 2D photonic crystal cavity in sequence.

reference. A Rabi frequency of 7 MHz is observed with a fitted decay time $T_{Rabi} = 761 \pm 69$ ns, within which the spin can be coherently driven. In this case, T_{Rabi} is an effective timescale set by the Rabi pulses applied,

intrinsic spin dephasing, and spin energy relaxation in the host environment. In Fig.4i, when the left inner loop is turned on, crosstalk noise is introduced to the Rabi oscillation, resulting in a decreased T_{Rabi} to $249 \pm$

42 ns. The large decrease in T_{Rabi} is expected under strong random driving noise and matches simulations (Supplementary Section I). However, we observe in Fig.4j that when both the left inner and outer loop are on and operated out-of-phase, the Rabi oscillation is protected, with T_{Rabi} tripled in duration to 704 ± 103 ns, meaning that the coherence of the qubit control returns to the case without the neighbouring drive field (within the range of error bars). From the recovery of the T_{Rabi} value, one can estimate the extinction ratio of the crosstalk microwave power to be 0.03 (-15 dB, Supplementary Section I). In comparison, in Fig.4k, when the signals in the left inner and outer loops are in phase, the noise is considerably increased, with $T_{Rabi} = 162 \pm 30$ ns. Our results show that the crosstalk mitigation effectively removes the noise generated by the neighbouring control line. The same level of noise attenuation in our case would require a qubit detuning of 40 MHz (Supplementary Section J) where a finite-size frequency band for each qubit imposes architectural complexity, requiring generation of large gradient field at scale [24].

Conclusions

We have demonstrated a site-defined control architecture using foundry microelectronics, for the scalable manipulation of spin qubits. With NVs lithographically positioned at predefined sites, we showed that their associated electron spin can be driven efficiently, important for quantum computing, which requires liquid helium operation to extract coherent photons from NVs, and hence has limited thermal budget. Most importantly, our results demonstrate that crosstalk in driving adjacent spins can be strongly mitigated through an active cancellation scheme, without significantly sacrificing this driving efficiency. The scheme works without frequency detuning spin qubit transitions [24–26], allowing distinct control of sets of identical qubits. The extinction ratio of field cancellation can also be improved by precisely balancing the driving of the inner and outer loops (see Methods).

Foundry microelectronics also gives access to mature silicon device libraries. In combination with photonic integrated circuits, a large-scale spin-photon interfaced quantum information processor could be realised, overcoming space and energy constraints. In Fig.5(a), we present an exemplar multi-purpose device combining CMOS-compatible integrated photonics and multi-layer electronics for solid-state spin systems. We show in Fig.5(b) that besides spin driving, one could realise static field tuning [27], electrical spin readout [28, 29], photon detection, and logical electronics [30] in the same platform. The loop structure we present in the work (Fig.2(a)), with the central 10 μm region, is compatible with out-of-plane photonics (Fig.5(c-d)), such as bullseye gratings [31] or solid immersion lenses [32]. With the 2 μm exit, our

structures can also be combined with in-plane photonics (Fig.5(e-f)) such as waveguides [33] and photonic crystal nanocavities [34, 35]. Photonic accessibility provided by this scheme would greatly enhance the single photon collection efficiency and the coherent extraction of single photons.

Our demonstration consists of spin sites separated by 60 μm , limited by the 0.13 μm process node. However, it is possible to pursue higher densities at smaller process nodes by exploiting the presented crosstalk cancellation scheme. Considering demonstrated NV positioning accuracy of several hundreds nanometers [33] and a sub-micron optical modes through confocal microscopy or waveguide mode excitation [36], 1 μm separation should be achievable. The scheme presented here is also translatable to alternative quantum platforms that use microwave driving, including other colour centres in diamond [37], single spin molecules [38], quantum dots [39] or superconducting circuits [40].

Methods

Device fabrication

We employ the 0.13 μm IHP-SG13G2 BiCMOS technology with two thick metal layers for current-carrying applications and five thin metal layers for interconnections. The track width of the inner (outer) loops are 5.5 μm (4 μm), both on the same 2 μm thick aluminium layer. We follow the lithography method in Ref. [33] for nanodiamond positioning on the chip. Nanodiamonds are sized around 50 nm diameter, milled from high pressure high temperature diamond (Nabond). First, a post-process inductively coupled plasma etch is used to release the inner region of the device, creating a 5 μm -deep trench. This allows nanodiamonds to be positioned at the centre of the loops. A layer of polymethyl methacrylate (PMMA) is then coated and patterned by electron beam lithography (Raith Voyager). This create sites on the PMMA mask on which the nanodiamond (suspended in methanol) is then dropcast. Removing the PMMA then results in nanodiamonds positioned precisely on the predefined sites.

Experimental setup

A scanning confocal microscope is used to optically address the NV in this work. With a 0.9 numerical aperture microscope objective (Olympus M Plan N 100x/0.90NA), the excitation beam (515 nm, Cobolt 06-MLD) is focused on the sample at a nearly diffraction-limited spot ($< 1 \mu\text{m}$ diameter). The NV photoluminescence is collected through the same lens and separated from the excitation path using a dichroic mirror. By using a high NA objective, the NV PL is extracted from the background fluorescence such as scattering from metal layers. Electronically, for

the active cancelling demonstration, the microwave source (Rohde & Schwarz SMB100AP20) is split by a power splitter (Mini-Circuits ZN2PD2-63-S+) for driving the inner and outer right metallic loop interface. On one path, an additional tunable power attenuator (Mini-Circuits RCDAT-6G-120H) and phase shifter (Vaunix LPS-802) are applied. Both paths are amplified (Microwave Amplifiers Ltd AM4-2-6-43-43R) and fed to an isolator (DiTom Microwave D3C2040) before the device-under-test. Timetagging and pulsing are recorded by UQDevices Logic-16 and Swabian Instruments Pulse Streamer 8/2. The electronic setup for crosstalk-mitigated spin control only differs with another random phase shifter applied before power splitting. Pulsing is achieved using a microwave switch (Mini-Circuits, ZASW-2-50DR+, DC-5 GHz) in Rabi oscillation measurements. Full electronic circuits are shown in Supplementary Fig.S6.

Electron spin Rabi oscillations and CW-ODMR measurements

We perform electron spin Rabi oscillations by driving the NV ground state triplets ($|0\rangle_e$ and $|\pm 1\rangle_e$). Fig.3a shows the corresponding pulse sequences. The electron spin is first polarised into the $|0\rangle_e$ state by a 3 μ s long 515 nm laser pulse. A microwave pulse of length τ is then applied to resonantly drive the transition between $|0\rangle_e \longleftrightarrow | + 1\rangle_e$ (with the ground state zero-field splitting around 2.87 GHz). In our measurement, an external static magnetic field is applied using a strong permanent magnet in order to lift the degeneracy of the two transitions ($|0\rangle_e \longleftrightarrow | + 1\rangle_e$ and $|0\rangle_e \longleftrightarrow | - 1\rangle_e$) and to shift the resonances such that it is best matched to the on-chip loop resonance (Supplementary Section E). Another laser pulse of 3 μ s is used to readout the spin state by the PL intensity (stronger in the $|0\rangle_e$ state and weaker in the $|\pm 1\rangle_e$ state due to state-dependent intersystem crossing). The PL intensity is extracted by summing the photon count in the first 0.5 μ s interval and normalising to the count summed over the last 1.5 μ s. We use the same laser pulse to polarise and readout the electron state. In Fig.3b-j, the Rabi measurements are presented (in the y-axis) with the relative intensity normalised between ± 1 for comparison. For the Rabi oscillation results presented in Fig.4h-k, the error in decay time is deduced from the variance of the parameter estimation during fitting, presenting one standard deviation error. The slight drift in oscillation is an artifact due to device heating under microwave power.

In the continuous-wave ODMR measurement, the 515 nm laser is constantly on while the frequency of the microwave source is swept around the resonance of electron spin transitions. Again, due to the difference of PL intensity for the electron states, a dip is observed at resonances with a certain depth (the ODMR contrast). For results shown in Fig.4a-e, the contrast is

extracted by fitting the measured PL intensity across frequency sweeps to a Gaussian dip. Error bars, showing one standard deviation in photon counts, arise from the photon shot noise and low drift of the experimental setup.

Extinction ratio of crosstalk field

The field cancellation extinction ratio (directly proportional to the residual crosstalk field) is undetectable (within experimental error bar) from the CW-ODMR measurements (Fig.4c-e) and Rabi oscillation lifetimes (Fig.4h-k) directly. Fitting the results, a -15 dB extinction ratio of crosstalk field power is inferred. The extinction ratio can be further improved by precisely balancing the driving of the inner-outer loops to the optimal ratio. For our case demonstrated in Fig.4(h-k), a -20 dB imbalance of microwave power (from the left loops) at the NV would diminish T_{Rabi} only by 2% under the active cancelling protection and a -30 dB imbalance for 0.2% (Supplementary Section I).

Acknowledgements. The authors thank J. Monroy-Ruz for building the confocal microscope used in this experiment and S. Komrakova and J. Frazer for fabrication support. The authors thank J. Monroy-Ruz and J. Matthews for useful discussions. The authors acknowledge funding support from the Quantum Computing and Simulation Hub Partnership Resource Project RFSQ and the Engineering and Physical Sciences Research Council (EPSRC) grant QC:SCALE EP/W006685/1.

References

- [1] Arute, F., Arya, K., Babbush, R., Bacon, D., Bardin, J.C., Barends, R., Biswas, R., Boixo, S., Brandao, F.G., Buell, D.A., *et al.*: Quantum supremacy using a programmable superconducting processor. *Nature* **574**(7779), 505–510 (2019)
- [2] Zhong, H.-S., Wang, H., Deng, Y.-H., Chen, M.-C., Peng, L.-C., Luo, Y.-H., Qin, J., Wu, D., Ding, X., Hu, Y., *et al.*: Quantum computational advantage using photons. *Science* **370**(6523), 1460–1463 (2020)
- [3] Evered, S.J., Bluvstein, D., Kalinowski, M., Ebadi, S., Manovitz, T., Zhou, H., Li, S.H., Geim, A.A., Wang, T.T., Maskara, N., *et al.*: High-fidelity parallel entangling gates on a neutral-atom quantum computer. *Nature* **622**(7982), 268–272 (2023)
- [4] Kjaergaard, M., Schwartz, M.E., Braumüller, J., Krantz, P., Wang, J.I.-J., Gustavsson, S., Oliver, W.D.: Superconducting qubits: Current state of play. *Annual Review of Condensed Matter Physics* **11**, 369–395 (2020)

- [5] Gambetta, J.: IBM’s roadmap for scaling quantum technology. IBM Research Blog (September 2020) (2020)
- [6] Bravyi, S., Dial, O., Gambetta, J.M., Gil, D., Nazario, Z.: The future of quantum computing with superconducting qubits. *Journal of Applied Physics* **132**(16) (2022)
- [7] Kurizki, G., Bertet, P., Kubo, Y., Mølmer, K., Petrosyan, D., Rabl, P., Schmiedmayer, J.: Quantum technologies with hybrid systems. *Proceedings of the National Academy of Sciences* **112**(13), 3866–3873 (2015)
- [8] Ristè, D., Fallek, S., Donovan, B., Ohki, T.A.: Microwave techniques for quantum computers: State-of-the-art control systems for quantum processors. *IEEE Microwave Magazine* **21**(8), 60–71 (2020)
- [9] Bardin, J.C., Slichter, D.H., Reilly, D.J.: Microwaves in quantum computing. *IEEE Journal of Microwaves* **1**(1), 403–427 (2021)
- [10] Brecht, T., Pfaff, W., Wang, C., Chu, Y., Frunzio, L., Devoret, M.H., Schoelkopf, R.J.: Multilayer microwave integrated quantum circuits for scalable quantum computing. *npj Quantum Information* **2**(1), 1–4 (2016)
- [11] Lekitsch, B., Weidt, S., Fowler, A.G., Mølmer, K., Devitt, S.J., Wunderlich, C., Hensinger, W.K.: Blueprint for a microwave trapped ion quantum computer. *Science Advances* **3**(2), 1601540 (2017)
- [12] Spring, P.A., Cao, S., Tsunoda, T., Campanaro, G., Fasciati, S., Wills, J., Bakr, M., Chidambaram, V., Shteynas, B., Carpenter, L., *et al.*: High coherence and low cross-talk in a tileable 3d integrated superconducting circuit architecture. *Science Advances* **8**(16), 6698 (2022)
- [13] Piltz, C., Sriarunothai, T., Varón, A., Wunderlich, C.: A trapped-ion-based quantum byte with 10–5 next-neighbour cross-talk. *Nature Communications* **5**(1), 4679 (2014)
- [14] Wang, H., Trusheim, M.E., Kim, L., Raniwala, H., Englund, D.R.: Field programmable spin arrays for scalable quantum repeaters. *Nature Communications* **14**(1), 704 (2023)
- [15] Clark, G., Raniwala, H., Koppa, M., Chen, K., Leenheer, A., Zimmermann, M., Dong, M., Li, L., Wen, Y.H., Dominguez, D., *et al.*: Nanoelectromechanical control of spin–photon interfaces in a hybrid quantum system on chip. *Nano Letters* (2024)
- [16] Pompili, M., Hermans, S.L., Baier, S., Beukers, H.K., Humphreys, P.C., Schouten, R.N., Vermeulen, R.F., Tiggelman, M.J., Santos Martins, L., Dirkse, B., *et al.*: Realization of a multinode quantum network of remote solid-state qubits. *Science* **372**(6539), 259–264 (2021)
- [17] Abobeih, M., Wang, Y., Randall, J., Loenen, S., Bradley, C., Markham, M., Twitchen, D., Terhal, B., Taminiou, T.: Fault-tolerant operation of a logical qubit in a diamond quantum processor. *Nature* **606**(7916), 884–889 (2022)
- [18] Bian, K., Zheng, W., Zeng, X., Chen, X., Stöhr, R., Denisenko, A., Yang, S., Wrachtrup, J., Jiang, Y.: Nanoscale electric-field imaging based on a quantum sensor and its charge-state control under ambient condition. *Nature Communications* **12**(1), 2457 (2021)
- [19] Smith, J., Monroy-Ruz, J., Rarity, J.G., C Balram, K.: Single photon emission and single spin coherence of a nitrogen vacancy center encapsulated in silicon nitride. *Applied Physics Letters* **116**(13) (2020)
- [20] Knowles, H.S., Kara, D.M., Atatüre, M.: Observing bulk diamond spin coherence in high-purity nanodiamonds. *Nature Materials* **13**(1), 21–25 (2014)
- [21] Mariani, G., Nomoto, S., Kashiwaya, S., Nomura, S.: System for the remote control and imaging of MW fields for spin manipulation in NV centers in diamond. *Scientific Reports* **10**(1), 4813 (2020)
- [22] Wang, P., Yuan, Z., Huang, P., Rong, X., Wang, M., Xu, X., Duan, C., Ju, C., Shi, F., Du, J.: High-resolution vector microwave magnetometry based on solid-state spins in diamond. *Nature Communications* **6**(1), 6631 (2015)
- [23] Dréau, A., Lesik, M., Rondin, L., Spinicelli, P., Arcizet, O., Roch, J.-F., Jacques, V.: Avoiding power broadening in optically detected magnetic resonance of single nv defects for enhanced dc magnetic field sensitivity. *Physical Review B* **84**(19), 195204 (2011)
- [24] Jakobi, I., Neumann, P., Wang, Y., Dasari, D.B.R., El Hallak, F., Bashir, M.A., Markham, M., Edmonds, A., Twitchen, D., Wrachtrup, J.: Measuring broadband magnetic fields on the nanoscale using a hybrid quantum register. *Nature Nanotechnology* **12**(1), 67–72 (2017)
- [25] Neumann, P., Kolesov, R., Naydenov, B., Beck, J., Rempp, F., Steiner, M., Jacques, V., Balasubramanian, G., Markham, M., Twitchen, D., *et al.*:

- Quantum register based on coupled electron spins in a room-temperature solid. *Nature Physics* **6**(4), 249–253 (2010)
- [26] Sekiguchi, Y., Matsushita, K., Kawasaki, Y., Kosaka, H.: Optically addressable universal holographic quantum gates on diamond spins. *Nature Photonics* **16**(9), 662–666 (2022)
- [27] Arai, K., Belthangady, C., Zhang, H., Bargill, N., DeVience, S., Cappellaro, P., Yacoby, A., Walsworth, R.L.: Fourier magnetic imaging with nanoscale resolution and compressed sensing speed-up using electronic spins in diamond. *Nature Nanotechnology* **10**(10), 859–864 (2015)
- [28] Bourgeois, E., Jarmola, A., Siyushev, P., Gulka, M., Hruby, J., Jelezko, F., Budker, D., Nesladek, M.: Photoelectric detection of electron spin resonance of nitrogen-vacancy centres in diamond. *Nature Communications* **6**(1), 8577 (2015)
- [29] Gulka, M., Wirtitsch, D., Ivády, V., Vodnik, J., Hruby, J., Magchiels, G., Bourgeois, E., Gali, A., Trupke, M., Nesladek, M.: Room-temperature control and electrical readout of individual nitrogen-vacancy nuclear spins. *Nature Communications* **12**(1), 4421 (2021)
- [30] Kim, D., Ibrahim, M.I., Foy, C., Trusheim, M.E., Han, R., Englund, D.R.: A CMOS-integrated quantum sensor based on nitrogen–vacancy centres. *Nature Electronics* **2**(7), 284–289 (2019)
- [31] Li, L., Chen, E.H., Zheng, J., Mouradian, S.L., Dolde, F., Schröder, T., Karaveli, S., Markham, M.L., Twitchen, D.J., Englund, D.: Efficient photon collection from a nitrogen vacancy center in a circular bullseye grating. *Nano Letters* **15**(3), 1493–1497 (2015)
- [32] Hadden, J., Harrison, J., Stanley-Clarke, A.C., Marseglia, L., Ho, Y.-L., Patton, B., O’Brien, J.L., Rarity, J.: Strongly enhanced photon collection from diamond defect centers under microfabricated integrated solid immersion lenses. *Applied Physics Letters* **97**(24) (2010)
- [33] Weng, H.-C., Monroy-Ruz, J., Matthews, J.C.F., Rarity, J.G., Balram, K.C., Smith, J.A.: Heterogeneous integration of solid-state quantum systems with a foundry photonics platform. *ACS Photonics* **10**(9), 3302–3309 (2023)
- [34] Smith, J.A., Clear, C., Balram, K.C., McCutcheon, D.P., Rarity, J.G.: Nitrogen-vacancy center coupled to an ultrasmall-mode-volume cavity: a high-efficiency source of indistinguishable photons at 200 K. *Physical Review Applied* **15**(3), 034029 (2021)
- [35] Uppu, R., Pedersen, F.T., Wang, Y., Olesen, C.T., Papon, C., Zhou, X., Midolo, L., Scholz, S., Wieck, A.D., Ludwig, A., *et al.*: Scalable integrated single-photon source. *Science Advances* **6**(50), 8268 (2020)
- [36] Bhaskar, M.K., Sukachev, D.D., Sipahigil, A., Evans, R.E., Burek, M.J., Nguyen, C.T., Rogers, L.J., Siyushev, P., Metsch, M.H., Park, H., *et al.*: Quantum nonlinear optics with a germanium-vacancy color center in a nanoscale diamond waveguide. *Physical Review Letters* **118**(22), 223603 (2017)
- [37] Castelletto, S., Boretti, A.: Silicon carbide color centers for quantum applications. *Journal of Physics: Photonics* **2**(2), 022001 (2020)
- [38] Gaita-Ariño, A., Luis, F., Hill, S., Coronado, E.: Molecular spins for quantum computation. *Nature Chemistry* **11**(4), 301–309 (2019)
- [39] Lawrie, W., Rimbach-Russ, M., Riggelen, F.v., Hendrickx, N., Snoo, S.d., Sammak, A., Scappucci, G., Helsen, J., Veldhorst, M.: Simultaneous single-qubit driving of semiconductor spin qubits at the fault-tolerant threshold. *Nature Communications* **14**(1), 3617 (2023)
- [40] Mitchell, B.K., Naik, R.K., Morvan, A., Hashim, A., Kreikebaum, J.M., Marinelli, B., Lavrijsen, W., Nowrouzi, K., Santiago, D.I., Siddiqi, I.: Hardware-efficient microwave-activated tunable coupling between superconducting qubits. *Physical Review Letters* **127**(20), 200502 (2021)